

Machine Learning Exciton Dynamics

Florian Häse,¹ Stéphanie Valteau,¹ Edward Pyzer-Knapp,¹ and Alán Aspuru-Guzik^{1,*}

¹*Department of Chemistry and Chemical Biology,
Harvard University, Cambridge, Massachusetts 02138, USA*

arXiv:1511.07883v1 [physics.chem-ph] 24 Nov 2015

* aspuru@chemistry.harvard.edu

ABSTRACT

Obtaining the exciton dynamics of large photosynthetic complexes by using mixed quantum mechanics/molecular mechanics (QM/MM) is computationally demanding. We propose a machine learning technique, multi-layer perceptrons, as a tool to reduce the time required to compute excited state energies. With this approach we predict time-dependent density functional theory (TDDFT) excited state energies of bacteriochlorophylls in the Fenna-Matthews-Olson (FMO) complex. Additionally we compute spectral densities and exciton populations from the predictions. Different methods to determine multi-layer perceptron training sets are introduced, leading to several initial data selections. In addition, we compute spectral densities and exciton populations. Once multi-layer perceptrons are trained, predicting excited state energies was found to be significantly faster than the corresponding QM/MM calculations. We showed that multi-layer perceptrons can successfully reproduce the energies of QM/MM calculations to a high degree of accuracy with prediction errors contained within 0.01 eV (0.5 %). Spectral densities and exciton dynamics are also in agreement with the TDDFT results. The acceleration and accurate prediction of dynamics strongly encourage the combination of machine learning techniques with ab-initio methods.

INTRODUCTION

Studying the exciton dynamics of large photosynthetic complexes, such as the Fenna-Matthews-Olson (FMO) and light-harvesting II (LHII) complexes, has been a topic of much theoretical and experimental interest in recent years [1–14]. The theoretical community has focused on employing and developing reduced models to understand and describe the dynamics of these complexes [2, 3, 5, 7, 10, 11, 13–30]. These models rely on the knowledge of a system Hamiltonian for the interacting chromophores as well as spectral densities to describe the coupling of chromophores to their environments (protein, solvent) [31]. Computing a system Hamiltonian or spectral density is an arduous computational task due to the large number of degrees of freedom in these complexes. The most detailed approaches used to obtain these quantities have been mixed quantum mechanics/molecular mechanics (QM/MM) or semi-classical simulations [32, 33]. In particular, one QM/MM approach which has become popular in recent years [6, 8, 34, 35] consists in propagating the nuclei in the electronic ground state of the photosynthetic complex. This approximation

ignores the change in electronic structure due to excitation of the chromophores. Subsequently, for a subset of time frames, excited state energies for the chromophores are computed using a quantum method such as time-dependent density functional theory (TDDFT) [8]. The energy trajectories are then employed to extract system-bath correlation functions and finally spectral densities to use in exciton dynamics.

The downside of this approach is the large computational cost. Long molecular dynamics (MD) equilibration times of several tens of nanoseconds are required [36, 37]. The typical computational scaling of MD codes with the system size N is $\mathcal{O}(N \cdot \log N)$ [38]. In contrast, TDDFT calculations scale as $\mathcal{O}(N^2)$ [39]. Very often calculations need to be repeated for identical chromophores in similar environments to account for the effect of small variations. For instance in the case of a single-point mutation typically one would need to rerun the entire set of simulations.

In this work we propose an alternative route: using multi-layer perceptrons, a special class of neural networks, to predict the excited state along a MD trajectory. Such approaches typically scale as $\mathcal{O}(N)$ and were found to perform significantly faster than TDDFT approaches. As a test system we consider the Fenna-Matthews-Olson (FMO) complex of *P. Aestuarii*. We use multi-layer perceptrons as fully connected neural networks to predict the values of the first singlet excited state for the chromophores. We train the neural networks on the excited state energies obtained from QM/MM calculations. Several sampling methods are used to select the training data for the neural networks. In particular we tested a sampling method based on correlations of nuclear positions to improve on the spectral density predictions. Once trained, the neural networks are employed to make excited state energy predictions. Then one can build a Hamiltonian from the predictions and compute the exciton dynamics.

With optimal neural network training and 12 trained neural networks per BChl we predicted excited state energies with errors contained to 0.01 eV (0.5 %) from the neural network ensemble average. Further, with neural networks trained on data based on correlation sampling we correctly predict the shape of the spectral density and observe an error which is squared with respect to the excited state prediction error. This demonstrates the power of machine learning in chemistry, as has also been found in recent work where neural networks were employed to extract other chemical properties [40–44].

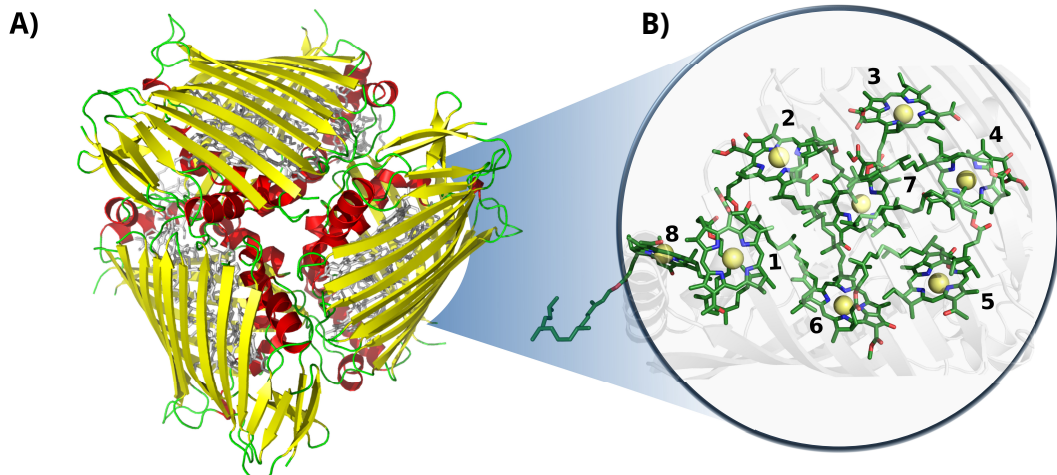


Figure 1. Crystal structure of the FMO complex in *P. Aestuarii* (PDB: 3EOJ [49]). (A) 3EOJ trimer crystal structure. (B) BChls' geometric arrangement in monomer A (residues 360 to 367, corresponding to sites 1 to 8). Hydrogens are not shown in this representation.

METHODS AND COMPUTATIONAL DETAILS

A. Ground state QM/MM simulations

A semi-classical description of the FMO complex was obtained by combining ground state MD simulations with TDDFT calculations of the first singlet excited state, known as the Q_y state [45], at given molecular conformations along the time-dependent trajectories. The MD runs were carried out using the NAMD software package [46] with the AMBER99 force field (ff99SB) [47]. The BChl-a parameters employed are reported in Ref. [48]. The X-ray crystal structure of the FMO trimer in *P. Aestuarii* (PDB: 3EOJ [49], see Fig. 1) was chosen as initial configuration. The trimer was solvated using a TIP3P water box [50]. The minimum distance between the crystal structure and edges of the solvent box was taken to be 15 Å [37, 51]. The charge was neutralized by adding sodium ions. The total number of atoms in the system was 141624. The simulation was equilibrated for 40 ns and the production run was 40 ps long with a 2 fs time-step. Electrostatic interactions were calculated with the Particle-Mesh Ewald method. Shake constraints were used for all bonds containing hydrogen. Simulations were carried out at 300 K and 1 bar using a Langevin thermostat and a Langevin piston as implemented in NAMD.

The time-dependent Q_y excited ground state gaps of the BChl-a molecules were obtained using TDDFT with the PBE0 [52] functional within the Tamm-Dancoff approximation (TDA) [53] using

Q-Chem [54]. We employed the 3-21G basis set due to the high computational cost of these simulations. The Q_y excited state was taken to be the one with the largest oscillator strength and the orientation of the transition dipole was verified using the same methodology as in Refs. [37] and [55]. Excited state energy distributions are shown in the supplementary information (see Sec. I) and trajectories can be downloaded from [56]. Excited state energies were computed at every 4 fs of the production run. Some values were excluded based on the oscillator strength / angle criterion / failed convergence. The excluded values were at most 2.15 % of the full trajectory.

B. Machine Learning: neural networks training

1. Input data representation

Multi-layer perceptrons (neural networks) were used to predict quantum mechanical excited state energies of BChls in the FMO complex from the MD classical coordinate trajectory. Neural networks were trained in a supervised training scheme using the back propagation algorithm [57]. Excited state energies from the TDDFT calculations described previously were provided to the neural network as targets. BChl conformations were represented by Coulomb matrices as proposed in Ref. [43]. Both, input and target feature distributions, were rescaled to a zero mean and a unitary standard deviation prior to neural network training [58].

By using Coulomb matrices as input features, neural networks can be trained on a representation of BChls which is translation and rotation invariant. Coulomb matrices are particularly suitable to describe BChls in the FMO complex as these molecules do not undergo large conformational changes within time scales of several tens of picoseconds [36, 37, 59]. Coulomb matrices were adapted to account for external charges within and around the represented BChl. The electrostatic influence of particles in the environment N was described by adding additional Coulomb potential terms to the corresponding Coulomb matrix entries (see Eq. 1):

$$M_{ij} = \begin{cases} Z_i^{2.4}/2 + \sum_{n \in N} \frac{Z_i Z_n}{|\vec{r}_i - \vec{r}_n|} & \text{for } i = j, \\ \frac{Z_i Z_j}{|\vec{r}_i - \vec{r}_j|} + \sum_{n \in N} \frac{Z_i Z_n}{|\vec{r}_i - \vec{r}_n|} + \sum_{n \in N} \frac{Z_j Z_n}{|\vec{r}_j - \vec{r}_n|} & \text{for } i \neq j. \end{cases} \quad (1)$$

Partial charges Z_i of atoms in the system were taken from the system topology (Amber 99SB force field [47] and Ref. [48]). Studies have shown that the tails of the BChls have little influence

on the Q_y excited state energies [37, 60]. Thus, instead of representing the entire BChl in a Coulomb matrix, the phytol tail was neglected and only the 90 atoms closest to the magnesium in the BChls were represented in Coulomb matrices to reduce their dimensionality. We included all external partial charges present in the system to generate Coulomb matrices.

2. Neural network architecture, choice of BChl molecule and over-fitting

We chose to use multi-layer perceptrons (neural networks) with logistic activation functions and two hidden layers. This set-up has been shown to perform particularly well for supervised regression problems [61]. Optimal neural network hyperparameters were identified from a grid search. Both the learning rate and the number of neurons in the first and second hidden layer were varied to find the lowest deviations between predictions and target data.

Instead of performing the grid search on each BChl in the FMO complex individually, only the most representative BChl was used to determine optimal neural network hyperparameters to reduce the computational cost. We identified this BChl in terms of shared Coulomb matrix space. Coulomb matrices of all eight BChls were clustered and compared. We found that site 3 shares the most Coulomb matrix space with all other sites (see supplementary information Sec. F).

From the grid search, we found that a learning rate of 10^{-4} with 204 neurons in the first hidden layer and 192 neurons in the second hidden layer results in the smallest average absolute deviation of predicted and target excited state energies.

Target feature over-fitting was avoided by using *early stopping* [62]. For all training sessions a total of 4000 trajectory frames was assigned to the training set as a balance between information and computational cost. Neural networks were trained on Intel(R) Xeon(R) CPUs (X5650 @ 2.67 GHz). Training one neural network on four cores took about (23.9 ± 5.0) h. Training times for other investigated training set sizes ranging from 500 to 5000 frames are reported in the supplementary information (see Sec. G).

3. Reducing training set redundancies through clustering: taxicab, Frobenius and “correlation” clustering

We employed different methods to select Coulomb matrices and corresponding excited state energies for neural network training. In a first approach training set Coulomb matrices were drawn

randomly from the entire trajectory as proposed in Ref. [62]. This led to excited state energy predictions with an average accuracy of 13 meV.

However, as BChl conformations in the data set are not uniformly distributed a training set consisting of randomly drawn Coulomb matrices likely contains redundant information. MD simulations were carried out in the NPT ensemble with constant temperature and pressure. Thus, the BChl conformations are sampled from a Boltzmann distribution [63]. To avoid selecting many similar conformations and thus similar Coulomb matrices we performed a cluster analysis on all Coulomb matrices of the entire trajectory to determine the most distinct Coulomb matrices. We implemented a Coulomb matrix cluster algorithm following the principles of the gromos method [64].

Distances between Coulomb matrices were measured using p-norms. Two different metrics were applied: $p = 1$ (taxicab norm) and $p = 2$ (Frobenius norm). Both clustering approaches resulted in more accurate predictions of excited state energies with accuracies of 9 meV but the prediction of exciton dynamics remained quite inaccurate (see Sec. E).

To improve the prediction of exciton dynamics, we developed a clustering method based on coordinate correlations in the classical MD trajectory. We will refer to this approach as the “*correlation*” clustering method. The Q_y state in BChls is mostly distributed along one of the diagonals which connects opposite nitrogen atoms [37]. Training set frames were thus selected based on high correlations in the nitrogen root-mean square deviation (RMSD). In particular, for the n -th BChl we sampled from

$$|C_n^{\text{RMSD}}(t)|^2 = |\langle D_n^{\text{Nitrogen}}(t) D_n^{\text{Nitrogen}}(0) \rangle|^2. \quad (2)$$

until 4000 frames with the largest RMSD correlation were selected. Here, $D_n^{\text{Nitrogen}}(t) = \sqrt{\frac{1}{4} \sum_{i=1}^4 \|\vec{r}_{n,i}(t) - \vec{r}_{n,i}(0)\|^2}$ refers to the root-mean square difference in position of the four nitrogen atoms in the n -th BChl at a given time t with respect to their position in the energy minimized crystal structure at time $t = 0$. This sampling led to a more accurate prediction of the spectral density (see Sec. E).

C. Exciton dynamics and spectral densities

To further compare the predicted excited state energy trajectories with the TDDFT trajectories we computed the exciton dynamics in the FMO complex using two different methods. The first is a stochastic integration of the Schrödinger equation as used in Ref. [8]. The second method is

the Markov Redfield master equation [65]. Both of the methods are Markovian but the first relies only on the excited state energy trajectories while the latter also depends on the spectral density. Here we focus on the sensitivity of these methods to the changes related to using neural networks rather than to more subtle questions on dynamics such as those addressed by the comparison of Markovian with non Markovian methods (e.g. the hierarchy equation of motion approach [2]).

Finally the spectral density $j(\omega)$, as used in the Redfield equations of motion, is obtained by normalizing the Fourier transform of the two-time correlation function as we discussed in Valleau et al. in Ref. [31]:

$$j(\omega) = \frac{J^{\text{harm}}(\omega)}{\pi} \quad \text{with} \quad J^{\text{harm}}(\omega) = \frac{\beta \hbar \omega}{2} \int_{-\infty}^{\infty} e^{i\omega t} C^{\text{cl}}(t). \quad (3)$$

The superscript “harm” refers to the harmonic prefactor which is needed to connect the QM/MM results to the open quantum system approach. Here $C^{\text{cl}}(t)$ denotes the classical correlation function as defined in Ref. [31].

RESULTS AND DISCUSSION

D. Excited state energy prediction using neural networks

1. Acceleration of excited state energy computations with neural networks

Intel(R) Xeon(R) CPUs (X5650 @ 2.67 GHz) were used to train neural networks and predict excited state energies. A total of 12 neural networks was trained for each of the eight BChls in monomer A of the FMO complex. Predictions of each of the 12 neural networks per BChl were averaged in a neural network ensemble averaging approach to obtain a more accurate prediction for the excited state energy trajectory. The spread of predictions of individual neural networks is given in the supplementary information (see Sec. H).

Training sets were generated with all four training set selection methods (see Sec. B 3). Predicting Q_y excited state energies for the entire trajectory (10^4 frames) for one BChl with one neural network took on average (3.9 ± 0.8) s on one core. In contrast, the quantum chemistry calculations using the TDDFT (PBE0/3-21G) model chemistry required approximately 60000 h for the entire trajectory on one core. Required calculation times to compute excited state energy trajectories for each of the eight BChls in the FMO complex are reported in Tab. I.

Method	Training [h]			Calculation [h]	Total [h]
	$t_{\text{Coul}}^{\text{input}}$	$t_{\text{E}}^{\text{target}}$	t_{train}	t_{Calc}	t_{tot}
PBE0/3-21G	-	-	-	480000	480000
NN _{Corr}	48	192000	9178	< 0.1	201226

Table I. Time required to compute excited state energies (10000 frames) for all eight bacteriochlorophylls (BChls) for TDDFT (PBE0/3-21G) and neural network (NN) predictions from correlation clustered Coulomb matrices. Reported times include neural network training (t_{train}) with input ($t_{\text{Coul}}^{\text{input}}$) and target feature ($t_{\text{E}}^{\text{target}}$) generation, excited state calculations/predictions (t_{Calc}) and the total time (t_{tot}). If trained neural networks are available, only Coulomb matrices need to be calculated for neural network predictions, reducing the required time to 48 h. Reported times correspond to training a total of 12 neural networks independently to obtain ensemble averaged excited state energies. All reported times refer to calculations on a single core of an Intel(R) Xeon(R) CPU (X5650 @ 2.67 GHz).

If trained neural networks are available, excited state energies of given BChl conformations can be predicted directly from Coulomb matrices representing the BChl conformations. Thus, to obtain the excited state energies of an entire trajectory consisting of 10000 frames, Coulomb matrices need to be calculated first. With a calculation time of 2.19 s per Coulomb matrix on one Intel(R) Xeon(R) CPU (X5650 @ 2.67 GHz) core, about 6 h are needed to compute all 10000 Coulomb matrices. With excited state energy predictions requiring less than a minute, excited state energy trajectories can be obtained from neural networks about four orders of magnitude faster compared to TDDFT calculations.

2. Accuracy of neural network predictions

As can be seen in Fig. 2 the ensemble average of 12 neural network predictions agrees well with the TDDFT data. Predictions from the average over 12 networks deviate from TDDFT values by ~ 0.3 meV regardless of the site and the input selection method. When considering excited state energies predicted from a single network, we observed a deviation of $\sigma_{s,\text{random}}^{\text{single}} < 14$ meV for all sites s when the neural network was trained on randomly drawn Coulomb matrices. This prediction error can be decreased to $\sigma_{s,\text{taxicab}}^{\text{single}} < 9$ meV by selecting the training set based on the Coulomb matrix space clustering taxicab method (see Sec. B 3). Frobenius clustering showed

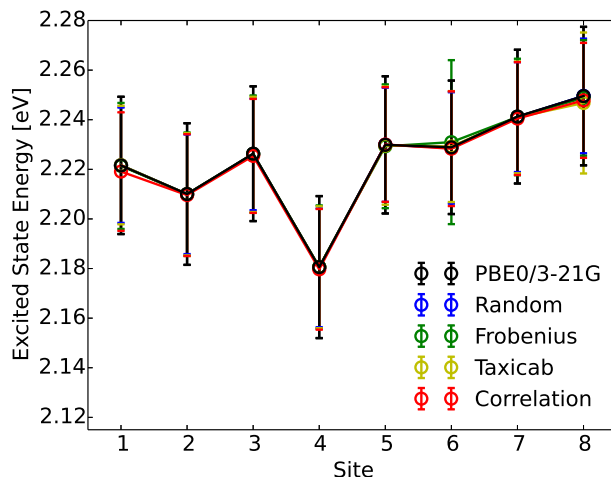


Figure 2. Mean and standard deviation of Q_y excited state energy distributions for all eight sites obtained from TDDFT calculations (PBE0/3-21G) and compared to neural network predictions. Neural networks were trained on Coulomb matrices selected from the classical MD trajectory by the indicated selection method. Error bars indicate the width of the excited state energy distribution.

similar deviations. In contrast, predictions from neural networks trained on correlation clustered Coulomb matrices show a slightly higher deviation of $\sigma_{s,\text{correlation}}^{\text{single}} < 15$ meV on average.

3. Cross-predictions: predicting excited state energies for other bacteriochlorophylls

Since all BChl-a molecules in the FMO complex consist of the same atoms and show similar geometrical conformations, we also used neural networks trained on one BChl to predict excited state energies of other BChls in the same monomer. This enabled us to understand how well the trained network can adapt to changes in the environment from changes in the Coulomb matrices. We observed that for any clustering method, the prediction error is about two times larger when performing this type of cross-prediction, see Fig. 3. Nonetheless, as we see in panel A, the largest observed average absolute deviation is still below 1.14 % (corresponding to 25 meV).

4. Predicting excited state energies of bacteriochlorophylls in other monomers

All neural networks were trained on BChl-a molecules in monomer A. These neural networks were then used to predict excited state energies of BChls in the other two FMO monomers. Each neural network predicted the excited state energies of the BChl corresponding to the one on which

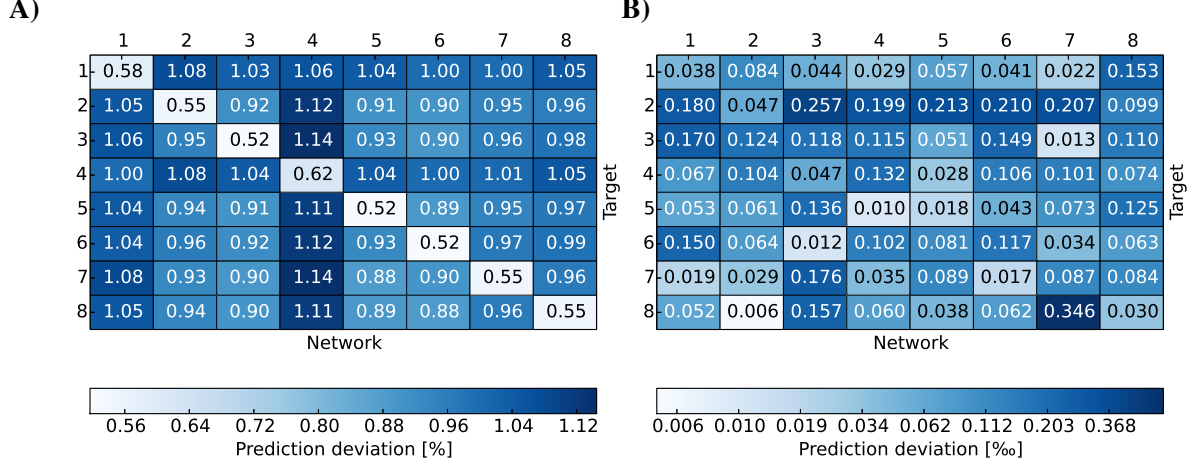


Figure 3. Relative absolute deviations of predicted excited state energies from TDDFT excited state energies. Neural networks trained on one particular site (indicated by “Network”) were used to predict excited state energies of another site (indicated by “Target”). Panel **A**) shows the relative absolute deviation $\bar{\sigma}_{\text{BChl}}^{\text{rel}}$ of predicted excited state energies from TDDFT excited state energies for each BChl, $\bar{\sigma}_{\text{BChl}}^{\text{rel}} = \sum_i |\epsilon_{\text{BChl}}^{\text{NN}}(t_i) - \epsilon_{\text{BChl}}^{\text{TDDFT}}(t_i)| / (N_{\text{frames}} \cdot \langle \epsilon_{\text{BChl}}^{\text{TDDFT}} \rangle)$, in percent. Panel **B**) shows the deviation $\sigma_{\text{BChl}}^{\text{mean}}$ of the mean of the predicted excited state energies from the mean of the TDDFT calculated excited state energies, $\sigma_{\text{mean}}^{\text{BChl}} = |\langle \epsilon_{\text{BChl}}^{\text{NN}} \rangle - \langle \epsilon_{\text{BChl}}^{\text{TDDFT}} \rangle| / \langle \epsilon_{\text{BChl}}^{\text{TDDFT}} \rangle$ in per-thousand.

it was trained (i.e. a neural network trained on site 1 in monomer A predicted site 1 in monomer B and C).

Due to the fact that the FMO complex is a homo-trimer, similar BChl conformations should be sampled during the MD simulation in each monomer. Thus, excited state energy averages are expected to be identical for corresponding BChls of different monomers, provided that the same phase space regions were covered in the simulation time. The results are presented in Fig. 4. In that figure, we show the time-averaged excited state energy predicted from 12 independently trained neural networks for each monomer as well as the time-averaged Q_y energies obtained from TDDFT for monomer A. The bars represent the spread of the distribution and not an error. The predicted distributions are narrower than the TDDFT distributions. This is probably due to the fact that frames corresponding to energies at the tails of the distribution are less sampled. Regarding the error on the other hand, the largest deviation encountered between mean values of excited state energy distributions is 3 meV.

We have found that trained neural networks can accurately predict TDDFT excited state ener-

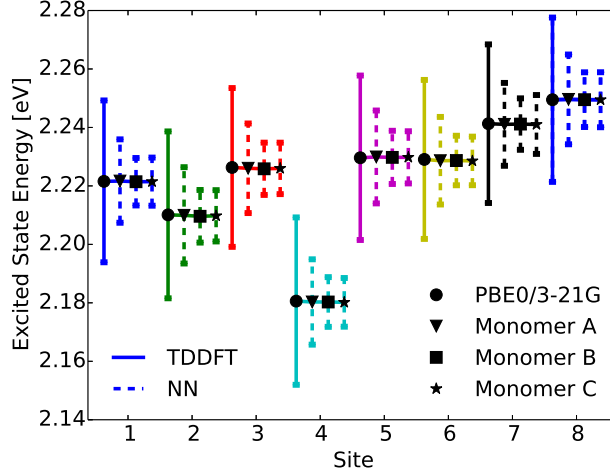


Figure 4. Mean and standard deviation of excited state energy distributions for all eight sites obtained using TDDFT PBE0/3-21G (solid line with circle), for monomer A, and using neural network prediction with training on 40% of all Coulomb matrices of monomer A for all three monomers (dashed lines and triangle, square and star symbol for monomers A, B, C). Error bars indicate the standard deviation of the obtained excited state energy distributions.

gies. This allows for a large reduction of computational time. It is possible to train on a single BChl and predict excited state energies of other BChls in the same monomer or in different monomers.

E. Spectral densities and exciton dynamics with neural networks

We then used the calculated excited state energy trajectories of all BChls to obtain information about interactions of the BChls with their environment by computing spectral densities. In addition, we built a Hamiltonian to extract the exciton dynamics in the system.

The spectral density $J^{\text{harm}}(\omega)$ (see Eq. 3) was computed for all eight sites in the FMO complex from the TDDFT excited state energies and neural network predicted excited state energies [31]. Spectral densities for each site were averaged over all BChls to obtain an averaged spectral density $J_{\text{ave}}(\omega)$. To minimize spurious effects in the Fourier transform, we multiplied the correlation function by a Gaussian of $\sigma^2 = 0.09 \cdot t_{\text{max}}^2$ with $t_{\text{max}} = 1600$ fs as done in Ref. [31]. The Gaussian is normalized to have unitary area in frequency domain so that in frequency domain this corresponds to a convolution with a Gaussian with a FWHM of 26cm^{-1} .

In Fig. 5 we show the comparison to our neural network prediction with training and prediction

on the same site and the various Coulomb matrix selection methods. We found that predicted spectral densities all have a shape which resembles the overall shape of the TDDFT spectral density. However, the height and accurate position of the peaks in the spectral density is most accurately predicted using correlation clustering.

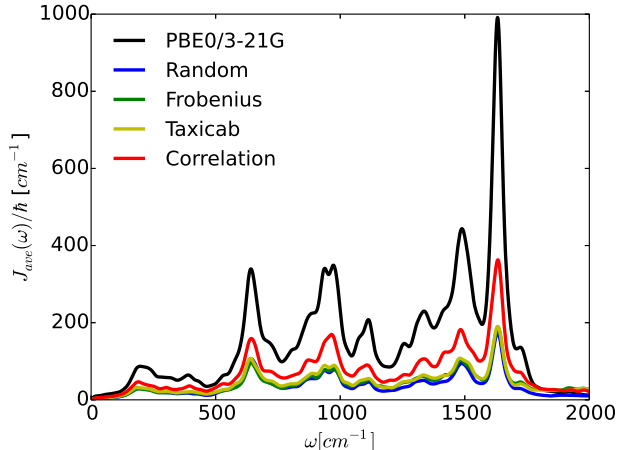


Figure 5. Spectral density averages $J_{\text{ave}}(\omega) = \sum_{\text{BChl}} J_{\text{BChl}}^{\text{harm}}(\omega)/N_{\text{BChl}}$. The spectral densities were computed from excited state energy trajectories obtained from TDDFT calculations (PBE0/3-21G) and compared to spectral densities from neural network predicted excited state energy trajectories. Neural networks were trained on the bacteriochlorophyll they predicted with the indicated Coulomb matrix selection method. The correlation method (see Sec. B 3) gives the best prediction.

Spectral densities for each BChl, calculated from TDDFT excited state energies and excited state energies predicted from neural networks trained on all input selection methods are plotted in the supplementary information (see Fig. 14 in Sec. J).

Average spectral densities were used to calculate the reorganization energy $\lambda = \int_0^\infty J_{\text{ave}}(\omega)/\omega d\omega$. Comparisons of reorganization energies are reported in Tab. II. We observe that the smallest deviation between neural network predicted results and TDDFT results occurs for neural networks trained on correlation clustered Coulomb matrices.

We also computed the population dynamics in the FMO complex monomer with a stochastic integration method [8]. We averaged 4000 stochastic trajectories to obtain converged population dynamics. The initial excited site was chosen to be site 1 and the dynamics was propagated for all eight coupled sites at 300 K. The couplings of the Hamiltonian were taken from Ref. [55, 66]. Results are shown in Fig. 6. We see that neural network predictions from neural networks trained on randomly drawn and correlation clustered Coulomb matrices predict the exciton dynamics in

Method (β)	Random	Frobenius	Taxicab	Correlation
σ_λ [%]	70.0	54.9	53.4	46.6

Table II. We report the percentage deviation of neural network predicted reorganization energies $\lambda_{\text{NN},\beta}$ from TDDFT (PBE0/3-21G) calculated reorganization energies λ_{TDDFT} as $\sigma_\lambda = |\lambda_{\text{TDDFT}} - \lambda_{\text{NN},\beta}|/\lambda_{\text{TDDFT}}$, where β indicates the method used for Coulomb matrix selections. Results are given in percent %.

agreement with TDDFT calculations.

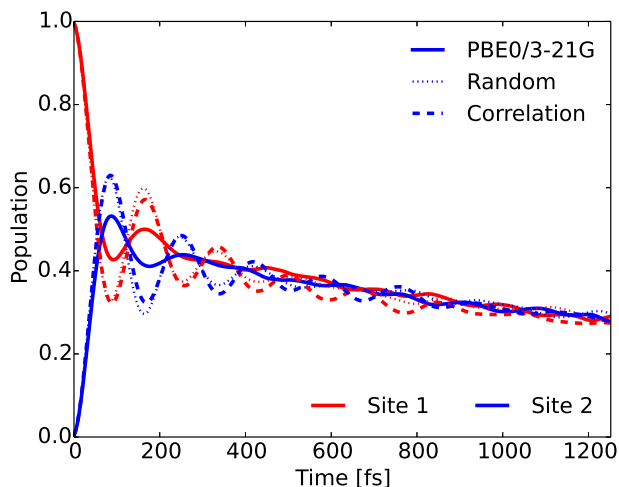


Figure 6. Population dynamics of the FMO complex calculated at 300 K with initial state in site 1. Here only two site populations are shown but dynamics was carried out for the 8 BChls. Excited state energy trajectories were obtained from TDDFT calculations (PBE0/3-21G) as well as neural networks trained on randomly drawn and correlation clustered Coulomb matrices.

We also employed the Markovian Redfield method to compute the exciton dynamics in the FMO complex (see Sec. C) [65]. In this case there is an explicit dependence of the exciton dynamics on the spectral density. The energies in the Hamiltonian were taken to be the averages from the TDDFT or neural network predicted excited state energy trajectories. The same couplings as for the stochastic integration method were used.

To investigate the importance of excited state energies and spectral densities on the Redfield exciton dynamics we calculated the exciton dynamics in two different ways. First, we computed the exciton dynamics with neural network predicted excited state energies and the average spectral density obtained from TDDFT calculations and then we used the neural network predicted energies as well as the neural network predicted spectral densities. Results are presented in Fig. 7 panel A,

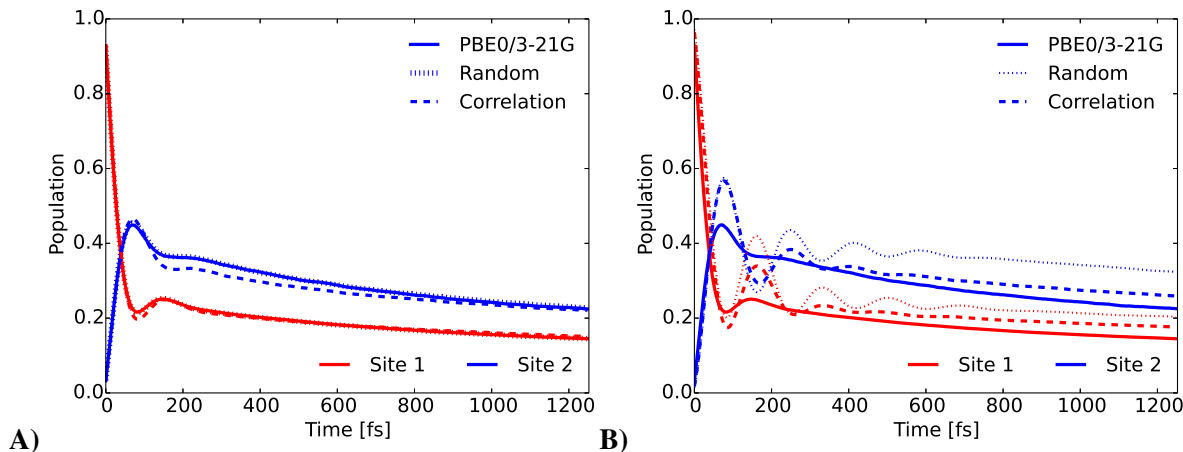


Figure 7. Time evolution of the exciton population for BChl 1 (red) and BChl 2 (blue) in the FMO complex calculated from excited state energy trajectories and average spectral densities using the Redfield method. The initial state is site 1 excited. Panel A) shows the exciton dynamics for neural network predicted excited state energies using the same TDDFT calculated average spectral density in all cases. Panel B) shows the exciton dynamics with both, excited state energy trajectories and harmonic average spectral densities predicted by neural networks trained with the indicated selection method.

for predicted excited state energies and TDDFT spectral densities and panel B, for excited state energies and spectral densities predicted by neural networks. We initialized the dynamics with the excitation in BChl 1 and propagated the dynamics for all eight coupled sites at 300 K.

In panel A we see that given a constant spectral density the error on energies is small and does not strongly influence the exciton dynamics. The main role is played by the spectral density as can be seen in panel B. Here we see much larger differences depending on the neural network sampling method and we notice that the prediction of neural networks trained on correlation clustered Coulomb matrices agrees better with the TDDFT exciton dynamics. Deviations of neural network predicted exciton dynamics from TDDFT calculated exciton dynamics are listed in detail in the supplementary information (see Sec. J). Further methods should be investigated to improve the prediction of the spectral density, the error on the energy should be reduced further by an order of magnitude to predict spectral densities with the optimal reorganization energy.

CONCLUSION

The computational study presented in this article showed that multi-layer perceptrons (neural networks) can be used to successfully predict excited state energies of BChls in the FMO complex. Using different methods to select a training data set for neural network training we were able to generate neural networks which can predict TDDFT excited state energies with high accuracy (0.01 eV). Furthermore, the neural networks can predict properties such as QM/MM derived spectral densities or exciton population dynamics. The prediction of excited state energies using the neural networks is about seven orders of magnitude faster than TDDFT. If we include training feature generations we still observe a speed-up of about four orders of magnitude. Even if neural networks need to be trained first, excited state energies are obtained in less than half the time needed for TDDFT.

Based on the observations we made on the FMO complex we recommend the following procedure to apply machine learning to predict excited state properties of other systems:

1. Represent all molecules of interest and their chemical environment with Coulomb matrices.
2. Obtain optimal neural network architectures from hyperparameter grid searches. In particular, it is important identify the most representative molecule in terms of the space which contains the features used for neural network predictions.
3. Determine an optimal training set. Training sets for neural networks with optimal network architecture can be generated by selecting Coulomb matrices based on properties which are related to the desired quantum mechanical properties. We observed that selecting Coulomb matrices which represent Coulomb matrix space clusters improves excited state energy predictions. However, these do not necessarily work well for dynamics.
4. Make predictions. To predict spectral densities and exciton dynamics with high accuracy, Coulomb matrices should be selected for the training set if they reveal high excited state energy correlations. We found that nitrogen RMSD correlations in the BChls are a good indicator for excited state energy correlations. Thus, we selected Coulomb matrices based on high nitrogen RMSD correlations. Of course this might be complicated for some molecules with very delocalized excited states.

In conclusion, this approach provides a gigantic speedup to ground state QM/MM. From a neural network trained on a single BChl molecule, we can predict the excited states of 23 other molecules

in the system at very low additional computational costs. This will be particularly useful to speed up or simply to enable the simulation of larger, more complex and challenging light-harvesting systems. Further, it will be helpful to study, for instance, the role of small changes in the environment of the exciton dynamics. Future questions we would like to address include the possibility of extending the prediction to other temperatures using for example multi-target machine learning.

ACKNOWLEDGMENTS

S.V. and A.A.-G. acknowledge support from the Center for Excitonics and Energy Frontier Research Center funded by the U.S. Department of Energy under award DE-SC0001088. Computations were run on the Harvard University’s Odyssey cluster, supported by the Research Computing Group of the FAS Division of Science.

-
- [1] Adolphs, J & Renger, T. (2006) How proteins trigger excitation energy transfer in the fmo complex of green sulfur bacteria. *Biophys. J.* **91**, 2778–2797.
 - [2] Ishizaki, A & Fleming, G. R. (2009) Theoretical examination of quantum coherence in a photosynthetic system at physiological temperature. *Proc. Natl. Acad. Sci.* **106**, 17255–60.
 - [3] Kreisbeck, C, Kramer, T, Rodriguez, M, & Hein, B. (2011) High-performance solution of hierarchical equations of motion for studying energy transfer in light-harvesting complexes. *J. Chem. Theory and Comput.* **7**, 2166–2174.
 - [4] Krueger, B. P, Scholes, G. D, & Fleming, G. R. (1998) Calculation of couplings and energy-transfer pathways between the pigments of lh2 by the ab initio transition density cube method. *J. Phys. Chem. B* **102**, 5378–5386.
 - [5] Mohseni, M, Rebentrost, P, Lloyd, S, & Aspuru-Guzik, A. (2008) Environment-assisted quantum walks in photosynthetic energy transfer. *J. Chem. Phys.* **129**, 174106.
 - [6] Olbrich, C & Kleinekathöfer, U. (2010) Time-dependent atomistic view on the electronic relaxation in light-harvesting system ii. *J. Phys. Chem. B.* **114**, 12427–12437.
 - [7] Plenio, M. B & Huelga, S. F. (2008) Dephasing-assisted transport: quantum networks and biomolecules. *New J. Phys.* **10**, 113019.
 - [8] Shim, S, Rebentrost, P, Valleau, S, & Aspuru-Guzik, A. (2012) Atomistic study of the long-lived

- quantum coherences in the fenna-matthews-olson complex. *Biophys. J.* **102**, 649 – 660.
- [9] Scholes, G. D, Curutchet, C, Mennucci, B, Cammi, R, & Tomasi, J. (2007) How solvent controls electronic energy transfer and light harvesting. *J. Phys. Chem. B* **111**, 6978–6982.
- [10] Sarovar, M, Fleming, G. R, & Wahley, K. B. (2010) Quantum entanglement in photosynthetic light-harvesting complexes. *Nat. Phys.* **6**, 462–467.
- [11] Moix, J, Wu, J, Huo, P, Coker, D, & Cao, J. (2011) Efficient energy transfer in light-harvesting systems, iii: The influence of the eighth bacteriochlorophyll on the dynamics and efficiency in fmo. *J. Phys. Chem. Lett.* **2**, 3045–3052.
- [12] Huo, P & Coker, D. F. (2010) Iterative linearized density matrix propagation for modeling coherent excitation energy transfer in photosynthetic light harvesting. *J. Chem. Phys.* **133**, 184108.
- [13] Cao, J & Silbey, R. J. (2009) Optimization of exciton trapping in energy transfer processes. *J. Phys. Chem. A* **113**, 13825–13838.
- [14] Wu, J, Liu, F, Shen, Y, Cao, J, & Silbey, R. J. (2010) Efficient energy transfer in light-harvesting systems, i: optimal temperature, reorganization energy and spatial-temporal correlations. *New J. Phys.* **12**, 105012.
- [15] Jang, S, Newton, M. D, & Silbey, R. J. (2007) Multichromophoric förster resonance energy transfer from b800 to b850 in the light harvesting complex 2: Evidence for subtle energetic optimization by purple bacteria. *J. Phys. Chem. B* **111**, 6807–6814.
- [16] Rebentrost, P, Mohseni, M, Kassal, I, Lloyd, S, & Aspuru-Guzik, A. (2009) Environment-assisted quantum transport. *New J. Phys.* **11**, 033003.
- [17] Ishizaki, A & Fleming, G. R. (2011) On the interpretation of quantum coherent beats observed in two-dimensional electronic spectra of photosynthetic light harvesting complexes. *J. Phys. Chem. B* **115**, 6227–6233.
- [18] Abramavicius, D & Mukamel, S. (2010) Quantum oscillatory exciton migration in photosynthetic reaction centers. *J. Chem. Phys.* **133**, 064510.
- [19] Skochdopole, N & Mazziotti, D. A. (2011) Functional subsystems and quantum redundancy in photosynthetic light harvesting. *J. Phys. Chem. Lett.* **2**, 2989–2993.
- [20] Ritschel, G, Roden, J, Strunz, W. T, Aspuru-Guzik, A, & Eisfeld, A. (2011) Absence of quantum oscillations and dependence on site energies in electronic excitation transfer in the fenna-matthews-olson trimer. *J. Phys. Chem. Lett.* **2**, 2912–2917.
- [21] Rebentrost, P & Aspuru-Guzik, A. (2011) Communication: Exciton-phonon information flow in the

- energy transfer process of photosynthetic complexes. *J. Chem. Phys.* **134**, 101103.
- [22] Singh, N & Brumer, P. (2011) Electronic energy transfer in model photosynthetic systems: Markovian vs. non-markovian dynamics. *Faraday Discuss.* **153**, 41–50.
- [23] Singh, N & Brumer, P. (2011) Non-markovian second-order quantum master equation and its markovian limit: Electronic energy transfer in model photosynthetic systems. *arXiv:1106.5911v1*.
- [24] Pachón, L. A & Brumer, P. (2012) Computational methodologies and physical insights into electronic energy transfer in photosynthetic light-harvesting complexes. *Phys. Chem. Chem. Phys.* **14**, 10094–10108.
- [25] Vlaming, S. M & Silbey, R. J. (2012) Correlated intermolecular coupling fluctuations in photosynthetic complexes. *J. Chem. Phys.* **136**, 055102.
- [26] Caruso, F, Saikin, S. K, Solano, E, Huelga, S, Aspuru-Guzik, A, & Plenio, M. B. (2012) Probing biological light-harvesting phenomena by optical cavities. *Phys. Rev. B* **85**, 125424.
- [27] Mohseni, M, Shabani, A, Lloyd, S, & Rabitz, H. (2011) Optimal and robust energy transport in light-harvesting complexes:(ii) a quantum interplay of multichromophoric geometries and environmental interactions. *arXiv:1104.4812v1*.
- [28] Zhu, J, Kais, S, Rebentrost, P, & Aspuru-Guzik, A. (2011) Modified scaled hierarchical equation of motion approach for the study of quantum coherence in photosynthetic complexes. *J. Phys. Chem. B.* **115**, 1531–1537.
- [29] de Vega, I. (2011) Non-markovian stochastic schrödinger description of transport in quantum networks. *Journal of Physics B: Atomic, Molecular and Optical Physics* **44**, 245501.
- [30] Roden, J, Eisfeld, A, Wolff, W, & Strunz, W. T. (2009) Influence of complex exciton-phonon coupling on optical absorption and energy transfer of quantum aggregates. *Phys. Rev. Lett.* **103**, 058301.
- [31] Valleau, S, Eisfeld, A, & Aspuru-Guzik, A. (2012) On the alternatives for bath correlators and spectral densities from mixed quantum-classical simulations. *J. Chem. Phys.* **137**, 224103.
- [32] Mercer, I. P, Gould, I. R, & Klug, D. R. (1999) A quantum mechanical / molecular mechanical approach to relaxation dynamics : Calculation of the optical properties of solvated bacteriochlorophyll-a. *J. Phys. Chem. B* **103**, 7720–7727.
- [33] Tao, G & Miller, W. H. (2010) Semiclassical description of electronic excitation population transfer in a model photosynthetic system. *J. Phys. Chem. Lett.* **1**, 891–894.
- [34] Olbrich, C, Jansen, T. L. C, Liebers, J, Aghtar, M, Strümpfer, J, Schulten, K, Knoester, J, & Kleinekathöfer, U. (2011) From atomistic modeling to excitation transfer and two-dimensional spectra

- of the fmo light-harvesting complex. *J. Phys. Chem. B* **115**, 8609–21.
- [35] Damjanović, A, Kosztin, I, Kleinekathöfer, U, & Schulten, K. (2002) Excitons in a photosynthetic light-harvesting system: A combined molecular dynamics, quantum chemistry, and polaron model study. *Phys. Rev. E* **65**, 031919.
- [36] Olbrich, C, Strümpfer, J, Schulten, K, & Kleinekathöfer, U. (2011) Quest for spatially correlated fluctuations in the fmo light-harvesting complex. *J. Phys. Chem. Lett.* **2**, 1771–1776.
- [37] Jurinovich, S, Curutchet, C, & Mennucci, B. (2014) The fenna-matthews-olson protein revisited: A fully polarizable (td)dft/mm description. *ChemPhysChem* **15**, 3194–3204.
- [38] Shan, Y, Klepeis, J. L, Eastwood, M. P, Dror, R. O, & Shaw, D. E. (2005) Gaussian split ewald: A fast ewald mesh method for molecular simulation. *J. Chem. Phys.* **122**, 054101.
- [39] Rappoport, D & Hutter, J. (2012) *Fundamentals of Time-Dependent Density Functional Theory (Lecture Notes in Physics 837)*. (Springer Berlin / Heidelberg), pp. 317–336.
- [40] Rupp, M, Tkatchenko, A, Müller, K.-R, & von Lilienfeld, O. A. (2012) Fast and accurate modeling of molecular atomization energies with machine learning. *Phys. Rev. Lett.* **108**, 058301.
- [41] Ramakrishnan, R, Hartmann, M, Tapavicza, E, & von Lilienfeld, O. A. (2015) Electronic spectra from tddft and machine learning in chemical space. *J. Chem. Phys.* **143**.
- [42] Hansen, K, Biegler, F, Ramakrishnan, R, Pronobis, W, von Lilienfeld, O. A, Müller, K.-R, & Tkatchenko, A. (2015) Machine learning predictions of molecular properties: Accurate many-body potentials and nonlocality in chemical space. *J. Phys. Chem. Lett.* **6**, 2326–2331.
- [43] Rupp, M, Tkatchenko, A, Müller, K.-R, & von Lilienfeld, O. A. (2012) Fast and Accurate Modeling of Molecular Atomization Energies with Machine Learning. *Phys. Rev. Lett.* **108**, 058301.
- [44] Pyzer-Knapp, E. O, Li, K, & Aspuru-Guzik, A. (2015) Learning from the harvard clean energy project: The use of neural networks to accelerate materials discovery. *Advanced Functional Materials* **25**, 6495–6502.
- [45] Olivucci, M. (2005) *Computational Photochemistry*. (Elsevier), pp. 93–128.
- [46] Phillips, J. C, Braun, R, Wang, W, Gumbart, J, Tajkhorshid, E, Villa, E, Chipot, C, Skeel, R. D, Kale, L, & Schulten, K. (2005) Scalable molecular dynamics with namd. *J. Comput. Chem.* **26**, 1781–1802.
- [47] Cornell, W. D, Cieplak, P, Bayly, C. I, Gould, I. R, Merz, K. M, Ferguson, D. M, Spellmeyer, D. C, Fox, T, Caldwell, J. W, & Kollman, P. A. (1995) A second generation force field for the simulation of proteins, nucleic acids, and organic molecules. *J. Am. Chem. Soc.* **117**, 5179–5197.
- [48] Ceccarelli, M, Procacci, P, & Marchi, M. (2003) An ab initio force field for the cofactors of bacterial

- photosynthesis. *J. Comput. Chem.* **24**, 129–142.
- [49] Tronrud, D, Wen, J, Gay, L, & Blankenship, R. (2009) The structural basis for the difference in absorbance spectra for the fmo antenna protein from various green sulfur bacteria. *Photosynthesis Research* **100**, 79–87.
- [50] Jorgensen, W. L & Madura, J. D. (1983) Solvation and conformation of methanol in water. *J. Am. Chem. Soc.* pp. 1407–1413.
- [51] Olbrich, C, Strümpfer, J, Schulten, K, & Kleinekathöfer, U. (2011) Quest for spatially correlated fluctuations in the fmo light-harvesting complex. *J. Phys. Chem. B* **115**, 758–764. PMID: 21142050.
- [52] Perdew, J. P, Ernzerhof, M, & Burke, K. (1996) Rationale for mixing exact exchange with density functional approximations. *J. Chem. Phys.* **105**, 9982–9985.
- [53] Taylor, J. C. (1954) Tamm-dancoff method. *Phys. Rev.* **95**, 1313–1317.
- [54] Shao, Y, Gan, Z, Epifanovsky, E, Gilbert, A. T. B, Wormit, M, Kussmann, J, Lange, A. W, Behn, A, Deng, J, Feng, X, Ghosh, D, Goldey, M, Horn, P. R, Jacobson, L. D, Kaliman, I, Khaliullin, R. Z, Kúš, T, Landau, A, Liu, J, Proynov, E. I, Rhee, Y. M, Richard, R. M, Rohrdanz, M. A, Steele, R. P, Sundstrom, E. J, Woodcock III, H. L, Zimmerman, P. M, Zuev, D, Albrecht, B, Alguire, E, Austin, B, Beran, G. J. O, Bernard, Y. A, Berquist, E, Brandhorst, K, Bravaya, K. B, Brown, S. T, Casanova, D, Chang, C.-M, Chen, Y, Chien, S. H, Closser, K. D, Crittenden, D. L, Diedenhofen, M, DiStasio Jr., R. A, Dop, H, Dutoi, A. D, Edgar, R. G, Fatehi, S, Fusti-Molnar, L, Ghysels, A, Golubeva-Zadorozhnaya, A, Gomes, J, Hanson-Heine, M. W. D, Harbach, P. H. P, Hauser, A. W, Hohenstein, E. G, Holden, Z. C, Jagau, T.-C, Ji, H, Kaduk, B, Khistyayev, K, Kim, J, Kim, J, King, R. A, Klunzinger, P, Kosenkov, D, Kowalczyk, T, Krauter, C. M, Lao, K. U, Laurent, A, Lawler, K. V, Levchenko, S. V, Lin, C. Y, Liu, F, Livshits, E, Lochan, R. C, Luenser, A, Manohar, P, Manzer, S. F, Mao, S.-P, Mardirossian, N, Marenich, A. V, Maurer, S. A, Mayhall, N. J, Oana, C. M, Olivares-Amaya, R, O'Neill, D. P, Parkhill, J. A, Perrine, T. M, Peverati, R, Pieniazek, P. A, Prociuk, A, Rehn, D. R, Rosta, E, Russ, N. J, Sergueev, N, Sharada, S. M, Sharma, S, Small, D. W, Sodt, A, Stein, T, Stück, D, Su, Y.-C, Thom, A. J. W, Tsuchimochi, T, Vogt, L, Vydrov, O, Wang, T, Watson, M. A, Wenzel, J, White, A, Williams, C. F, Vanovschi, V, Yeganeh, S, Yost, S. R, You, Z.-Q, Zhang, I. Y, Zhang, X, Zhou, Y, Brooks, B. R, Chan, G. K. L, Chipman, D. M, Cramer, C. J, Goddard III, W. A, Gordon, M. S, Hehre, W. J, Klamt, A, Schaefer III, H. F, Schmidt, M. W, Sherrill, C. D, Truhlar, D. G, Warshel, A, Xue, X, Aspuru-Guzik, A, Baer, R, Bell, A. T, Besley, N. A, Chai, J.-D, Dreuw, A, Dunietz, B. D, Furlani, T. R, Gwaltney, S. R, Hsu, C.-P, Jung, Y, Kong, J, Lambrecht, D. S, Liang,

- W, Ochsenfeld, C, Rassolov, V. A, Slipchenko, L. V, Subotnik, J. E, Van Voorhis, T, Herbert, J. M, Krylov, A. I, Gill, P. M. W, & Head-Gordon, M. (2015) Advances in molecular quantum chemistry contained in the q-chem 4 program package. *Mol. Phys.* **113**, 184–215.
- [55] Chandrasekaran, S, Aghtar, M, Valteau, S, Aspuru-Guzik, A, & Kleinekathöfer, U. (2015) Influence of force fields and quantum chemistry approach on spectral densities of bchl a in solution and in fmo proteins. *J. Phys. Chem. B* **119**, 9995–10004. PMID: 26156758.
- [56] Häse, F, Valteau, S, Pyzer-Knapp, E, & Aspuru-Guzik, A. (2015) Machine learning for exciton dynamics: Qy trajectories, <http://dx.doi.org/10.6084/m9.figshare.1611141>. *figshare*.
- [57] Rumelhart, D. E, Hinton, G. E, & Williams, R. J. (1986), eds. Rumelhart, D. E, McClelland, J. L, & PDP Research Group, C. (MIT Press, Cambridge, MA, USA), pp. 318–362.
- [58] Heaton, J. (2015) Encog: Library of interchangeable machine learning models for java and c#. *Journal of Machine Learning Research* **16**, 1243–1247.
- [59] von Lilienfeld, O. A, Ramakrishnan, R, Rupp, M, & Knoll, A. (2015) Fourier series of atomic radial distribution functions: A molecular fingerprint for machine learning models of quantum chemical properties. *International Journal of Quantum Chemistry* **115**, 1084–1093.
- [60] List, N. H, Curutchet, C, Knecht, S, Mennucci, B, & Kongsted, J. (2013) Toward reliable prediction of the energy ladder in multichromophoric systems: A benchmark study on the fmo light-harvesting complex. *Journal of Chemical Theory and Computation* **9**, 4928–4938.
- [61] Riedmiller, M. (1994) Advanced supervised learning in multi-layer perceptrons - from backpropagation to adaptive learning algorithms. *Computer Standards & Interfaces* **16**, 265–278.
- [62] Prechelt, L. (1998) Automatic early stopping using cross validation: quantifying the criteria. *Neural Networks* **11**, 761 – 767.
- [63] Frenkel, D & Smit, B. (2002) *Understanding Molecular Simulation*. (Academic Press), pp. 165–199.
- [64] Daura, X, Gademann, K, Jaun, B, Seebach, D, van Gunsteren, W. F, & Mark, A. E. (1999) Peptidfaltung: Wenn die simulation das experiment erreicht. *Angewandte Chemie* **111**, 249–253.
- [65] Breuer, H.-P & Petruccione, F. (2002) *The Theory of Open Quantum Systems*. (Oxford University Press, New York).
- [66] Aghtar, M, Strümpfer, J, Olbrich, C, Schulten, K, & Kleinekathöfer, U. (2013) The fmo complex in a glycerol-water mixture. *J. Phys. Chem. B* **117**, 7157–7163. PMID: 23697741.

SUPPLEMENTARY INFORMATION

F. Coulomb matrix space cluster analysis: choosing the best grid-search BChl molecule

The neural networks were trained on Coulomb matrices representing BChl conformations generated during the classical MD simulation in a supervised training-scheme. TDDFT excited state energies were used as training target. To design an optimal neural network architecture with a minimal deviation between predictions and targets, a grid search on several neural network hyperparameters was performed. Learning rate and number of neurons in the first and second hidden layer were changed step-wise, as reported in Sec. G.

We found that BChls in the FMO complex show a high Coulomb matrix space overlap throughout the entire MD trajectory (see Fig. 8). By determining the site with the highest Coulomb matrix space overlap with all other sites we were therefore able to limit the number of grid searches for optimal neural network hyperparameters to one. Optimal neural network hyperparameters obtained for the most representative site with the highest Coulomb matrix space overlap were used for all other sites.

To identify the most representative site we first started a cluster analysis on all Coulomb matrices representing site 1 based on the gromos method [64]. Coulomb matrix distances were measured with the Frobenius norm (see Sec. B 3). The clustering cut-off was chosen to be $90 \text{ e}^2/\text{\AA}$ to clearly distinguish Coulomb matrices. Then, for all other sites, distances of all Coulomb matrices of all frames in the MD trajectory to all Coulomb matrices representing on particular cluster were calculated. If the distance was below the cut-off, the Coulomb matrix was attributed to the cluster. The pool of remaining Coulomb matrices was again clustered with the same method as site 1.

Coulomb matrix space overlap of one site with all other sites was then estimated by counting the number of Coulomb matrices of the considered site and of Coulomb matrices of all other sites in every individual cluster. Whenever two sites i and j contributed to the same cluster different numbers of Coulomb matrices n_i and n_j , the smaller number of Coulomb matrices $\min(n_i, n_j)$ was added to the Coulomb matrix space overlap estimation of both sites. This summation was carried out over all sites and all clusters. Quantitative results are presented in Fig. 8.

We observed that of all BChls in the FMO complex, site 3 has the most shared Coulomb matrix space with all other sites. However, the difference of shared Coulomb matrix space volumes is small. The highest observed value (34.19 % for site 3) is only about 10 % greater than the smallest

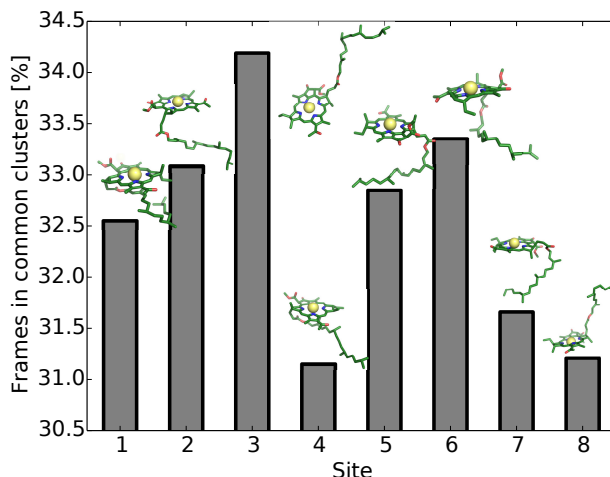


Figure 8. Common Coulomb matrix space regions of bacteriochlorophylls observed during the 40 ps production run. We report the number of frames (in %) of one site contributing to Coulomb matrix space clusters shared with at least one other site (cluster cut-off: $90 \text{ e}^2/\text{\AA}$). Stick representations of corresponding representative geometries of each individual site are shown for comparison.

observed value (31.15 % for site 4) and for every site about one third of all Coulomb matrices lies in shared Coulomb matrix space regions. Hence, we expect neural network architectures optimized on one site to also work well for all other sites. This assumption was confirmed by the similarity in prediction accuracy of neural networks trained on different sites (see Sec. D).

G. Neural network parameter grid search: finding the best network architecture

The prediction accuracy of a neural network is highly influenced by its architecture. Introducing hidden layers to the neural network architecture allows for the distinction of data which is not linearly separable. In this study we used multi-layer perceptrons (i.e. fully connected neural networks with at least one hidden layer) with two hidden layers and logistic activation functions. Several neural networks with different learning rates and numbers of neurons in the first and second hidden layer were designed and trained on Coulomb matrices and corresponding excited state energies. We used the back-propagation algorithm and a supervised training scheme with excited state energies as target. Overfitting was avoided with the early stopping method (see Sec. B). Thus we determined an optimal set of hyperparameters to identify a neural network architecture suitable for accurate excited state energy predictions for BChls in the FMO complex from classical MD

simulations.

The entire grid search was performed on BChl 3, which was shown to represent the most of the Coulomb matrix space covered by all BChl molecules in the FMO complex during the 40 ps production run (see Sec. F). Since optimal neural network architectures were not known beforehand we chose particular initial hyperparameter values prior to the grid search. Unless specified otherwise neural networks were trained with a learning rate of 10^{-3} and 180 neurons in the first and second hidden layer. Neural networks were trained on 3000 frames to keep the training times during the grid search reasonably small.

Learning rate

To determine an optimal learning rate we set up five different neural networks with learning rates of: 10^{-3} , $5 \cdot 10^{-4}$, 10^{-4} , $5 \cdot 10^{-5}$ and 10^{-5} . All of these neural networks were trained on 30 % of all trajectory frames representing BChl 3 by Coulomb matrices. The neural networks were designed with two hidden layers consisting of 180 respectively.

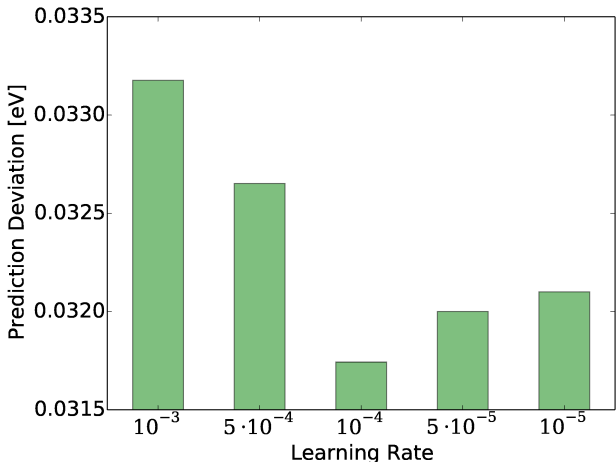


Figure 9. Average absolute deviations of predicted excited state energies from TDDFT excited state energies for neural networks with different learning rates. Neural networks were trained on 3000 Coulomb matrices randomly drawn from the 10000 frame data set. A learning rate of 10^{-4} resulted in the lowest prediction error. However, prediction error for other learning rates are less than 10 % larger than the minimal value.

The average absolute deviations of predicted excited state energies from TDDFT results for each neural network are depicted in Fig. 9. We see that deviations of single predicted excited state energies from TDDFT excited state energies ranges from 31.8 meV for a learning rate of 10^{-4} to

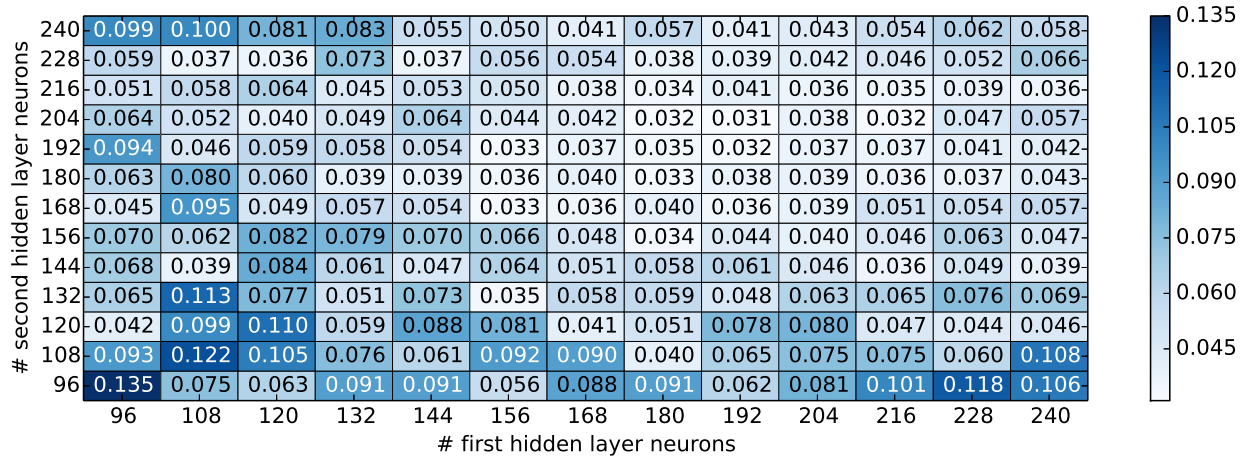


Figure 10. Average absolute deviations of predicted excited state energies from TDDFT calculated excited state energies for different numbers of neurons in the first and second hidden layer. Deviations are reported in eV. Neural networks were trained on 3000 Coulomb matrices randomly drawn from the 10000 frame data set. A hidden layer combination of 204 neurons in the first hidden layer and 192 neurons in the second hidden layer resulted in the smallest deviation of 31 meV.

33.2 meV for a learning rate of 10^{-3} . In any case, we found that the prediction error increases as the learning rate deviates from 10^{-4} . Hence, we consider a learning rate of 10^{-4} to be optimal for the case of excited state energies of BChls in the FMO complex. However, the small changes of the prediction accuracy with different applied learning rates indicates that the prediction accuracy of a neural network is not very sensitive to the learning rate for this application.

Choice of number of neurons

The influence of the number of neurons in the first and second hidden layer on the prediction accuracy of a neural network was investigated with several neural networks with a learning rate of 10^{-3} . Neuron numbers in each of the two hidden layers were varied from 96 to 240 in steps of 12. Each of the constructed neural networks was trained on site 3 with 3000 Coulomb matrices randomly selected from the 10000 frame data set. Results are illustrated in Fig. 10. The neural network with 204 neurons in the first hidden layer and 192 neurons in the second hidden layer showed the smallest average absolute deviation of 31 meV between single predicted excited state energies and TDDFT excited state energies.

Training set size [# frames]	Training time [h]
500	1.7 ± 0.6
1000	3.8 ± 1.4
1500	6.5 ± 2.8
2000	13.6 ± 6.5
2500	18.0 ± 7.9
3000	20.3 ± 5.5
3500	22.7 ± 7.3
4000	23.9 ± 5.0
4500	30.2 ± 1.5
5000	31.2 ± 4.8

Table III. Training times for neural network training on four cores. Each neural network was trained on Intel(R) Xeon(R) CPUs (X5650 @ 2.67 GHz) with 4 GB of RAM. Training set sizes are reported in number of frames randomly drawn from the 10000 frames of the trajectory of site 3. A total of 12 neural networks was trained on each training set size. Training times are reported with average and standard deviation of all neural network training sessions with the particular training set size.

Training set size

Aside from neural network hyperparameters we also investigated the effect of the number of Coulomb matrices in the training set on the prediction accuracy of the neural network. In general, the more data is provided to the neural network during training, the more accurately it can predict the targets. However, with the training set size the computational time spent on neural network training also increases. So we looked for a balance between the amount of data provided to the neural network during training and the computational cost of the neural network training.

Investigated training set sizes ranged from 500 Coulomb matrices to 5000 in steps of 500. In every case, Coulomb matrices of site 3 were drawn randomly from the 10000 frame data set. For each training set size a total of 12 neural networks was trained. Neural networks had a learning rate of 10^{-4} with 204 neurons in the first hidden layer and 192 neurons in the second hidden layer. Recorded training times for different training set sizes are reported in Tab. III as a 12 neural network average. Four cores of Intel(R) Xeon(R) CPUs (X5650 @ 2.67 GHz) with 4 GB of RAM

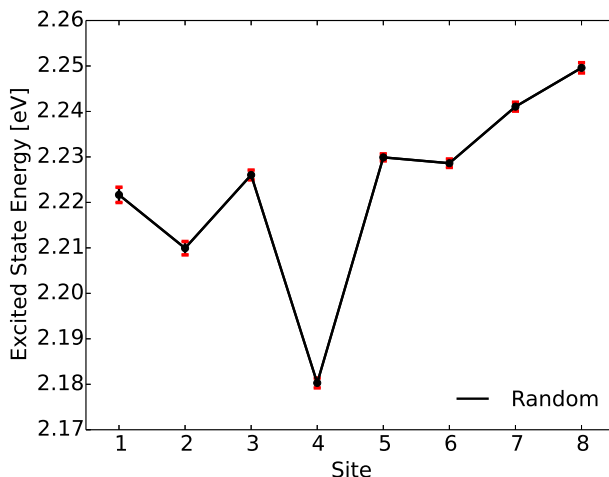


Figure 11. Averages of neural network predicted excited state energy trajectory averages. Error bars indicate the standard deviations of the neural network predicted excited state energy trajectory distributions. A total of 12 neural networks was trained for each of the eight sites on 4000 Coulomb matrices randomly drawn from the 10000 data frames of the indicated site.

were used to train one neural network.

We found that neural network training times significantly increase when including more than 4000 frames. Up to this training set size, neural network training takes about one day, which we considered a reasonable time for neural network training. Including 500 more frames to the training set increased the training time by about 6 h or 24 core hours. As a balance of the amount of input data and computational cost we therefore decided to use 4000 frames in the training set for neural network training.

H. Spread of neural network predictions

We used a total of 12 independent neural networks to predict excited state energies for a particular BChl in the FMO complex. Predicted trajectories of all 12 neural networks were averaged to obtain a more accurate predicted excited state energy trajectory. To justify the usage of the average of predicted excited state energy trajectories we report the spread of individual neural network predictions in Fig. 11. Neural networks with optimal hyperparameters (see Sec. G) were trained on 4000 Coulomb matrices randomly drawn from the 10000 frame data set for every respective site. After training, neural networks were used to predict the entire excited state energy trajectory of the site on which they were trained. Trajectory averages of predicted excited state averages

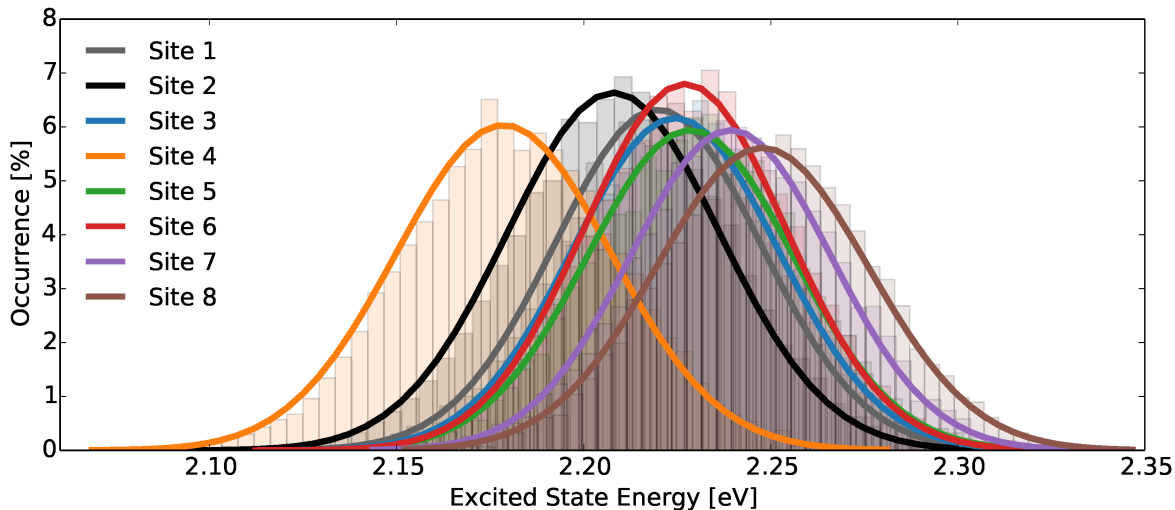


Figure 12. Excited state energy distributions for all eight BCHls in the FMO monomer A. Excited state energies were obtained from TDDFT calculations with the PBE0 functional and the 3-21G basis set. Distributions were calculated from a total of 10000 frames spanning 40 ps with a binning of 50.

were calculated for every neural network prediction. All predicted excited state energy trajectory averages were then ensemble averaged over the 12 neural networks trained on the particular site. Results are reported in Fig. 11 with the standard deviation of the neural network predicted excited state energy trajectory averages as error bars.

I. Excited state energy distributions

Excited state energies were calculated for all BChl in the FMO at every 4 fs of the 40 ps production run. Results were obtained from TDDFT calculations with the PBE0 functional and the 3-21G basis set using the Q-Chem quantum chemistry package. Distributions of the obtained excited state energy trajectories are depicted in Fig. 12.

J. Spectral Densities and Exciton Dynamics

Spectral Densities for individual sites

Spectral densities for individual BCHls in the FMO complex were calculated from TDDFT excited state energy trajectories and neural network predicted excited state energy trajectories.

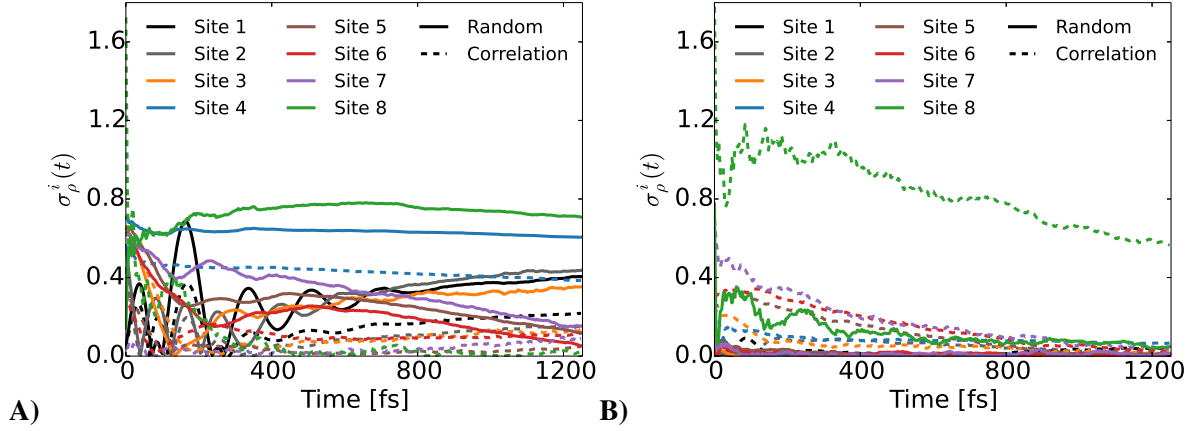


Figure 13. Deviation of TDDFT calculated exciton dynamics and neural network predicted exciton dynamics over time. The deviation was calculated as $\sigma_{\rho}^i(t) = |\rho_{ii}^{\text{TDDFT}}(t) - \rho_{ii}^{\text{NN}}(t)| / \rho_{ii}^{\text{TDDFT}}(t)$ with i indicating the BChl. Panel A) shows the deviation for exciton dynamics calculated with the Redfield method and neural network predicted harmonic average spectral densities. In Panel B), the TDDFT average spectral density was used for all calculations and neural networks only predicted excited state energy trajectories.

Neural networks were trained on Coulomb matrices selected with different selection methods from the 10000 frame trajectory. Harmonic spectral densities for individual BChls are shown in Fig. 14.

For the average spectral density (see Fig. 5 in Sec. E) we observed that neural networks trained on correlation clustered Coulomb matrices predicted spectral densities significantly better than any other Coulomb matrix selection method. However, the advantage of correlation clustering in terms of spectral density prediction accuracy is less obvious for spectral densities trained on individual BChls.

Nevertheless, for each of the introduced Coulomb matrix selection methods neural networks were able to predict the general shape of the spectral density, although the area below the curves is significantly smaller and correlation clustering identified more peaks than the other selection methods.

Error estimation of predicted exciton dynamics

The deviation of neural network predicted exciton dynamics and TDDFT calculated exciton dynamics of the i -th BChl was quantified by calculating $\sigma_{\rho}^i(t) = |\rho_{ii}^{\text{TDDFT}}(t) - \rho_{ii}^{\text{NN}}(t)| / \rho_{ii}^{\text{TDDFT}}(t)$. Deviations were calculated for the exciton dynamics obtained with the Redfield method as shown in Fig. 13.

We observe that for exciton dynamics calculations with neural network predicted average spectral densities (see panel A in Fig. 13) the error of neural networks trained on randomly drawn Coulomb matrices is significantly higher than the error of neural networks trained on correlation clustered Coulomb matrices. This behavior can be observed for all sites for times up to 1 ps. However, if we use the TDDFT calculated average spectral densities for all simulations instead of neural network predicted harmonic average spectral densities, we observe a much smaller error for neural networks trained on randomly drawn Coulomb matrices for all eight sites. This is due to the fact that the error on the energies is slightly smaller with the random sampling.

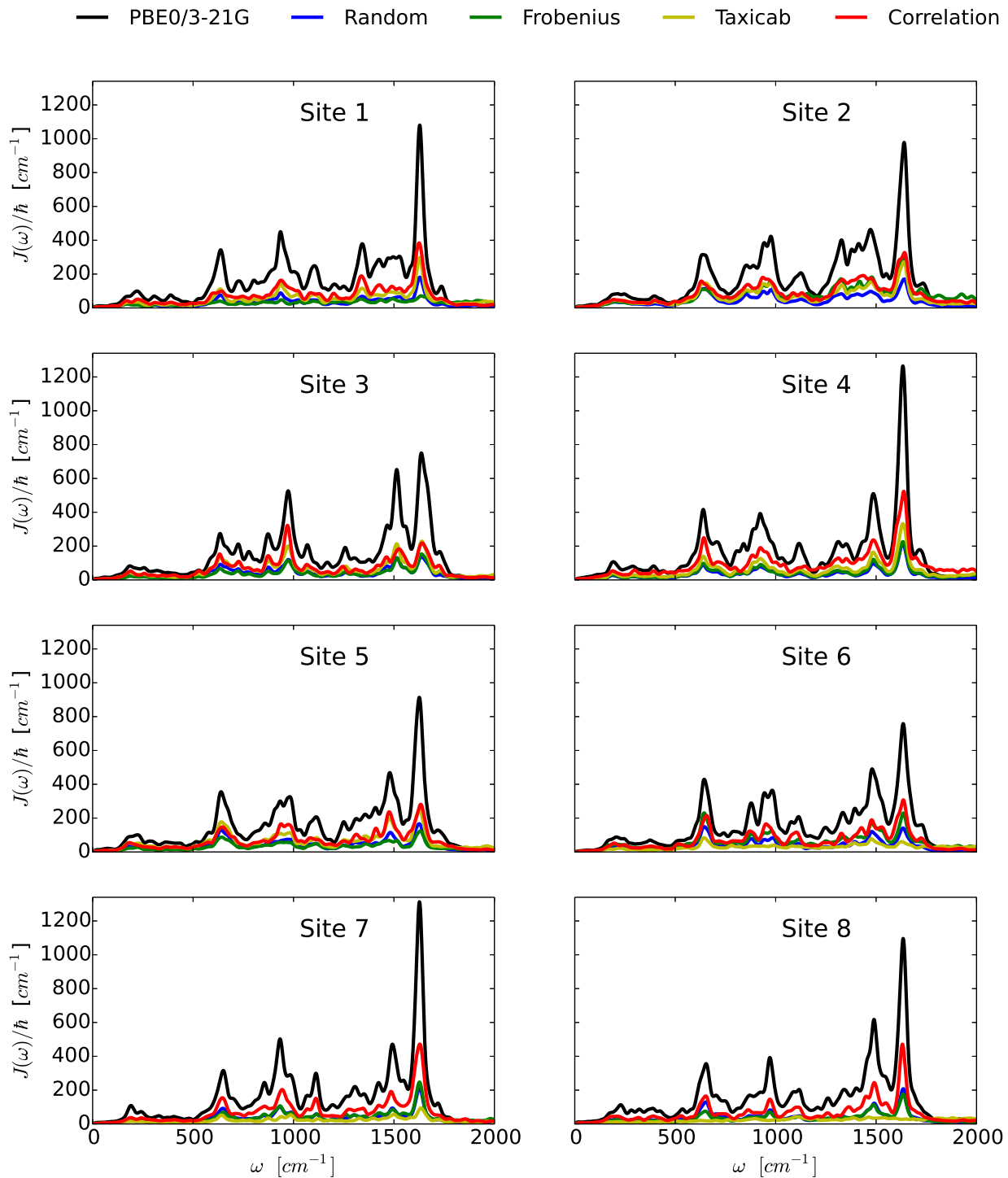


Figure 14. Harmonic spectral densities for individual sites in the FMO complex. The spectral densities were calculated from excited state energy trajectories obtained from TDDFT calculations (PBE0/3-21G) and compared to spectral densities from neural network predicted excited state energy trajectories. Neural networks were trained on the BChl they predicted with the indicated Coulomb matrix selection method.